Bioengineering a Miniaturized In Vitro 3D Myotube Contraction Monitoring Chip For Modelization of Muscular Dystrophies

Nicolas Rose[1], Surabhi Sonam[2,3], Thao Nguyen[2], Gianluca Grenci[4], Anne Bigot[1], Antoine Muchir[1], Benoît Ladoux*[2], Fabien Le Grand*[5], Léa Trichet*[6]

[1] Sorbonne Université, Inserm UMRS 974, Centre de Recherche en Myologie, 75013 Paris, France

[2] Institut Jacques Monod (IJM), Université de Paris, CNRS UMR 7592, Paris, France

[3] Current Affiliation: D Y Patil International University, Akurdi, Pune, 411044, India

[4] Mechanobiology Institute, National University of Singapore, Singapore

[5] Institut NeuroMyoGène, Université Claude Bernard Lyon 1, CNRS UMR 5310, INSERM U1217, 69008 Lyon, France

[6] Sorbonne Université, CNRS UMR 7574, Laboratoire de Chimie de la Matière Condensée de Paris, 75005 Paris, France

ABSTRACT

Quantification of skeletal muscle functional strength is essential to assess the outcomes of therapeutic procedures for muscular disorders. Several muscle three-dimensional "Organ-on-chip" models have been developed to measure the generated force. Yet, these technologies require a substantial amount of biological material, which is problematic in the context of limited patient sample.

Here we developed a miniaturized 3D myotube culture chip with contraction monitoring capacity. Combination of light-induced molecular adsorption technology and optimized micropatterned substrate design enabled to obtain high culture yields in tightly controlled physical and chemical microenvironments. Spontaneous twitch contractions in 3D myotubes derived from primary human myoblasts were observed, the generated force was measured and the contraction pattern characterized. In addition, the impact of three-dimensional culture on nuclear morphology was analyzed, confirming the similarity in organization between the obtained 3D myotubes and *in vivo* myofibers. Our system enabled to model *LMNA*-related Congenital Muscular Dystrophy (L-CMD) with successful development of mutant 3D myotubes displaying contractile dysfunction.

We anticipate that this technology shall be used to study contraction characteristics and evaluate how specific diseases affect muscle organization and force generation. Our downsized model system might allow to substantially improve drug screening capability for therapeutic oriented research.

1. Introduction

Skeletal muscles constitute the most prevalent tissue in the human body, representing more than half the corporal mass. Force generation relies on the contractile features of the myofibers constituting the muscle tissue. Myofibers are long multinucleated cells containing contractile myofibrils organized in periodic segments. These segments, called sarcomeres (Gautel and Djinović-Carugo, 2016), are composed of actin and myosin filaments parallel to the myofiber axis. Sliding of these myo-filaments along one another results in sarcomere shortening, and subsequent myofiber contraction (Powers et al., 2021).

Myofibers are terminally differentiated and cannot repair themselves in case of trauma. Yet, they host muscle stem cells (MuSCs) in niches between the myofiber membrane and the surrounding basal lamina (Evano and Tajbakhsh, 2018). After an acute injury or a mechanical overload, MuSCs contribute to the muscle regeneration in a process tightly regulated by physical and chemical constraints of the niche. Upon stimuli, MuSC will actively proliferate and most of their progeny will differentiate and fuse to form myotubes that will grow and generate new myofibers. In parallel, a fraction of activated MuSCs will return to the niche to renew the stem cell pool (Yin et al., 2013). Skeletal muscle tissue return to homeostasis following injury is classically evaluated by histology on cross-sections and force measurements as endpoints. As a complement to physiological symptoms analysis, there is a medical need to assess the muscle function in patients suffering muscular pathologies, for healthcare and research purposes (Iaizzo and Durfee, 2011). Indeed, muscle contraction is altered in the context of such rare dystrophies. Therefore, quantification of skeletal muscle functional strength is essential to estimate the outcomes of therapeutic procedures.

In skeletal muscle tissue, which primary function is force generation, assessing mechanical stresses and controlling the physical features of the environment is crucial during the different phases of myogenesis. The classical experimental tools to quantify forces generated by single cells include traction force microscopy (TFM) (Plotnikov et al., 2014)(Lo et al., 2000) (Balaban et al., 2001) or micropillar substrates (Tan et al., 2017) (Ghibaudo et al., 2011) (Trichet et al., 2012). The latter has been adapted to measure forces generated within 3D microtissues (Kural and Billiar 2013) (Boudou et

al., 2012) (Kalman et al., 2016) (Walker et al., 2018) (Legant et al., 2009). In the context of myotube formation, it appears as a well-adapted system. Indeed, the most common *in vitro* model used to study muscle is dish culture of myoblast monolayers, allowing studying early phases of myogenesis until myotube formation (Pimentel et al., 2017)(Zhang et al., 2020). However, when myotubes reach a certain level of maturation, contraction leads to detachment from the 2D culture substrates. Therefore, investigating myotube contraction requires to adapt 3D tissue force systems methods to measure myotube contractility.

Muscle cell contractile function, with resting tension and active generated forces during myotube fusion makes spatial control of the organoids particularly challenging (Osaki et al., 2020). Microfabricated substrates with patterned distribution of adhesive proteins represent a powerful tool to spatially constrain living cells (Théry, 2010) including myotube fusion and development (Charest et al., 2007). The use of micro- and nanopatterned grooves with linear striations promotes cell alignment (Kim et al., 2010) (Gorji et al., 2021) including the orientation of myocytes and cell fusion (Lam et al., 2006) (Huang et al., 2010). The most accessible adhesive proteins micropatterning techniques rely on a stamping approach, where non-printed areas are made non adhesive in a step further (Fink et al., 2007). However, these methods cannot be systematically adapted to substrates presenting complex 3D topographies, and alternative micropatterning technologies have been developed. In particular, light-induced molecular adsorption (LIMA) that consists in combining PLL-PEG polymers substrate passivation with UV local restoration of surface adhesion (Strale et al., 2016) can be used to homogeneously pattern surfaces having relief microfeatures even though this technique has not been yet implemented to skeletal muscle 3D organoids.

Powerful tools to perform therapeutical analysis (Rao et al., 2018) (Maffioletti et al., 2018) (Afshar et al., 2020) already exist, but their important sizes require a high number of myoblasts to generate organoids. “Organ-on-chip” and “tissue-on-chip” technologies are often used in the academic research and biotechnology industry, as for other tissue types (Ronaldson-Bouchard and Vunjak-Novakovic, 2018). They allow reducing the biological material prerequisite, by rescaling the dimensions of the organoids and expanding the number of replicates made from a constant initial sample size. Bioengineering research for such technology has already been performed, drastically

reducing the cell/construct ratio (Sakar et al., 2012) (Cvetkovic et al., 2014) (Mills et al., 2019) (Osaki et al., 2020).

In this work we propose a hydrogel free and well free system to diminish the size needed for a single tissue, and increase the pillar density on the silicone chip. To do so, the geometrical features of the pillars and proteins patterning technique were optimized to maximize the yields of 3D myotubes culture. This system enabled to monitor spontaneous contractions and study nuclei three-dimensional morphology of myotubes obtained from primary myoblasts as well as from healthy and L-CMD (LMNA-related Congenital Muscular Dystrophy) patients' immortalized myoblasts.

2. Materials & methods

2.1. Silicon wafer production and silanization

Silicon wafers were provided by the Mechanobiology Institute (National University of Singapore). The pillars and the grooves were produced in a two-step etching procedure. Briefly, silicon oxide wafers (300 nm thick, thermally grown) were initially patterned with the layout comprising of micro-grooves and the opening for the pillars. Then, in the first step of dry silicon etching the micro-grooves were protected by a patterned layer of photoresist, thus only the opening left to produce the pillars were etched down. A bosh-like process was used in an ICP reactor (SI500 RIE, Sentech, Germany) to etch the pillars cavities with vertical profiles. In the second etching step, the photoresist coating was removed and a second step of etching (same as before, but for shorter time) was then performed resulting in the fabrication of the micro-grooves together with reaching the final depth for the pillars cavities. Prior to PDMS casting, the silicon molds were coated with an anti-sticking layer of silane (1H,1H,2H,2H-perfluorooctyl-trichlorosilane 97%): after activation of the surface with O_2 plasma, the mold is immediately placed in a vacuum jar, a drop of the silane is added in a small container and the jar is evacuated for 15 min and left for 2 h for silane vapor deposition.

2.2. Polydimethylsiloxane chip molding

PDMS Sylgard 184 silicone elastomer base was mixed with curing agent in a 1:10 ratio (Dow Corning, ref 01673921). The mixture was poured on the silicon wafer, degased (with vacuum) and heated at 80°C for 2 h. PDMS was then peeled-off from the silicon wafer and cut into individual chips.

2.3. Matrigel micropatterning

Chips were hydrophilized by 5 min exposure to plasma cleaning. PLL-g-PEG (SuSoS Technology) was added to the chip surface for 1 h and rinsed three times with Phosphate-Buffered Saline (PBS). Photoactivable reagent (Alvéole's Classic PLPP 14.5 mg/mL) was added on the chip and specific areas were exposed with 1200 mJ/mm^2, using PRIMO micropatterning device (Alvéole) on 20X objective, with Leonardo photopatterning software (Alvéole). Following the photopatterning step, photoactivable reagent was vigorously rinsed away with PBS at least 5 times. Matrigel matrix (Corning ref 354230) solution (1mg/mL in DMEM) with 1:50 Cy5 dye-labeled fibronectin (conjugated in house using dialysis kit from Life technologies) was added on the chip and incubated for 1 h at room temperature. Matrigel solution was gently rinsed once with H_2O, and the patterned chips kept in sterile water at 4°C, plated in a multiwell-plate protected from the light.

2.4. Myoblasts lines and cell culture

Skeletal myoblasts cell lines were provided by the Myoline platform from the Institut de Myologie, Paris. The features of patients and muscles of origin are described in the **Supplementary table 1**. Cells were amplified in proliferation medium composed of DMEM (high glucose, GlutaMAX(TM), ThermoFischer scientific) with 16% 199 medium (Medium 199, GlutaMAX™ Supplement, ThermoFischer scientific), supplemented with 20% Fetal Bovine Serum (Gibco ref 15750-037), 5 ng/ml human epithelial growth factor (Life Technologies), 0.5 ng/ml bFGF (Life Technologies), 0.2 mM dexamethasone (Sigma-Aldrich), 25 µg/ml fetuin (Life Technologies), 5 µg/ml insulin (Life Technologies) and 0.5 µg/mL Gentamicine (Gibco). Cells were cultured directly in plastic

dishes and the passages were performed with 0.05% Trypsine-EDTA (1X) (Gibco). Human primary myoblasts were used within less than 30 divisions.

2.5. 3D myotube generation

The chips were rinsed with sterile PBS, plated in new sterile multiwell plates and immersed with proliferation medium. Myoblasts were plated (100k to 200k cells per chip depending on cell type - primary or immortalized, control or mutant, etc…) directly above the chip in a 0.5 to 1 mL proliferation medium drop. The chips were then spinned at 300g for 5 min, and left at 37°C for 1 h. The medium covering the chips was then gently changed (while keeping the chip immersed) 3 to 4 times until the off-pattern cells would detach. The chip was kept in proliferating conditions overnight until a switch to differentiation medium (DMEM high glucose, GlutaMAX (TM) + 0.1 mg/mL Gentamicine), by removing 1mL from the culture well and adding 1mL of new medium (repeated 4 to 5 times). The chips were left in differentiation conditions for at least 6 days (partial medium change can be done every 2 days), and 0.4 µm/mL recombinant rat Agrin (R&D systems) in differentiation medium was then added to the 3D myotubes. Fresh differentiation medium (1 mL) was gently added before contraction monitoring (performed after 7 to 14 days of differentiation).

2.6. Fixation and immunostaining

Samples were fixed 10 min with 4% Paraformaldehyde aqueous solution (Electronic Microscopy Sciences), blocked with 4% Bovine Serum Albumin (BSA) and permeabilized with 0.1% TritonX-100. The following primary antibodies (diluted in 4% BSA) were used for immunostaining: mouse IgG2b anti- Myosin Heavy Chain Type I MYH7 (DSHB, 1:50), rabbit monoclonal anti-Titin (DSHB 9D10-s, 1:500), mouse IgG1 anti-Sarcomeric Alpha Actinin (Abcam 9465, 1:500), rat monoclonal anti-Nicotinic Acetylcholine Receptor (Sigma-Aldrich, 1:800). The following secondary antibodies (diluted in PBS) were used for immunostaining: goat Alexa-Fluor-488/546/647-conjugated anti-mouse IgG1/IgG2b, anti-rabbit and anti-rat (Life Technologies, 1:500).

Actin was stained with Phalloidin-tetramethylrhodamine conjugate (Santa-Cruz 362065, 1:500) and nuclei with Hoechst 33342 (Life technologies H3570, 1:10,000). Chips were mounted upside down on glass coverslip with Dako Fluorescence Mounting medium (ref 53023).

For scanning electron microscopy preparation, samples were fixed first in a 4% paraformaldehyde solution and second using glutaraldehyde in a cacodylate/saccharose buffer for 1 h at 4 °C. After washing in a cacodylate/saccharose buffer the samples were dehydrated through successive ethanol baths with increasing concentrations and subsequently dried at the carbon dioxide critical point.

2.7. Microscopy imaging

Transmitted light videomicroscopy for contraction monitoring was performed at 37°C and 5% CO_2 on Nikon eclipse Ti microscope with coolsnap HQ2 camera and 20X objective. Fluorescent imaging was acquired with EVOS FL Cell Imaging System microscope (Life Technologies). Contraction force was calculated using Saez et al. 2007 formula (Saez et al., 2007). Confocal and 3D imaging was acquired with Nikon Ti2 microscope equipped with a motorized stage and a Yokogawa CSU-W1 spinning disk head coupled with a Prime 95 sCMOS camera (Photometrics). Scanning electron microscopy was performed with Hitachi SU-70 High vacuum FESEM 1 kV or 0.5 kV (high magnification) without coating.

- *2.8. Images and statistical analysis*

Images were acquired using Metamorph software and further treated with ImageJ/FIJI. Nuclear volumes were calculated by addition of all individually measured xy areas and multiplication with the confocal Z-step (zy or xz areas and ellipticities were not considered). All graphs and statistical analyses were performed with Prism software (tests and p-values are described in the legend of each figure).

3. Results

3.1. Downsized model for in vitro functional skeletal muscle culture.

The goal of this study was to create a 3D myotube culture chip with contraction monitoring capacity for therapeutical research. To this aim, we developed a method that consists in culturing human myoblasts amplified from patients' biopsies on microstructured substrates made in PDMS (Polydimethylsiloxane) **(Fig. 1A)**. The pre-molded PDMS chip micro-substrates (10x10mm) **(Fig. 1B**) allow to culture micro-tissues between micropillar duos at a high density (each chip can potentially bear 100 micro-tissues), providing numerous replicates while requiring relatively few myoblasts to be seeded (60k cells needed per chip). Pillar duos presented in between the pillars either a pattern of 6 µm periodic striations, with a height of 3.5 µm **(Fig. 1C)**, or no striation (controls). Different shapes, sizes and heights of the pillars were considered **(Fig. 1B,D,E and Supplementary table 2)**. Depending on their geometry, the pillars have different spring constant values (Saez et al., 2005), offering the possibility to adapt the resisting elastic force of the system to 3D myotube contraction.

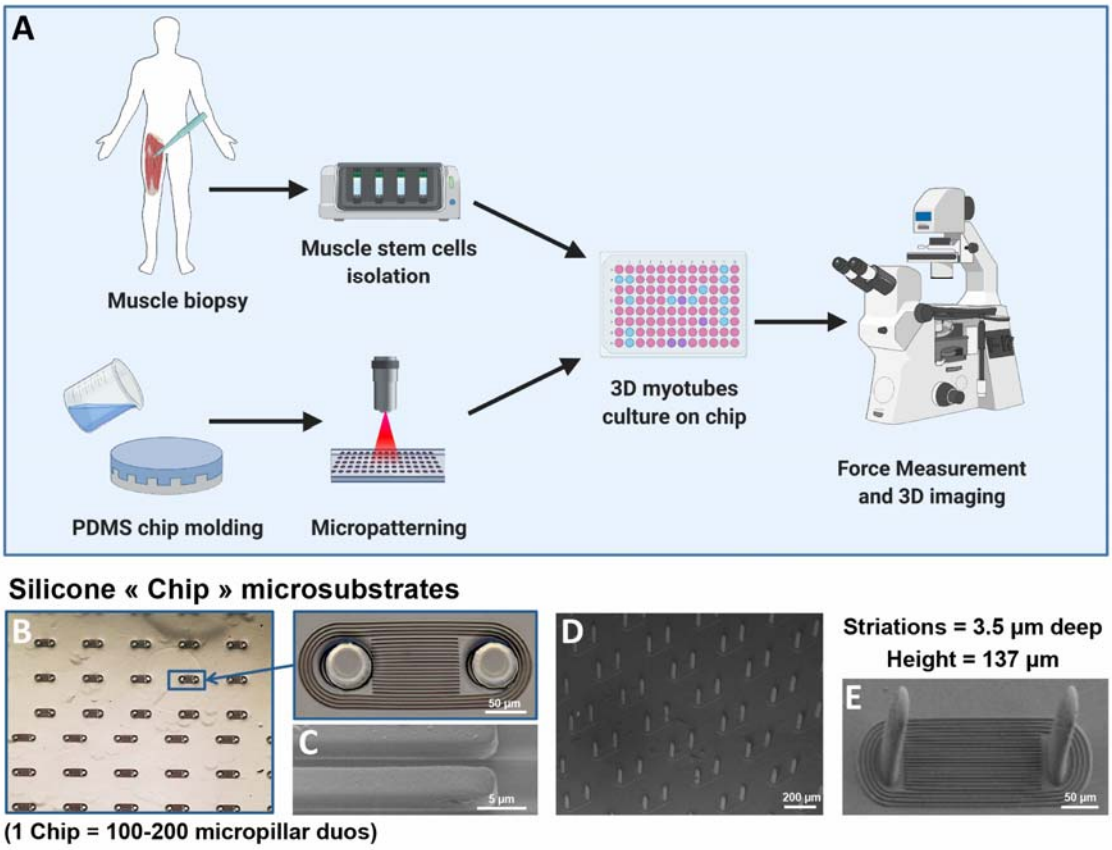

<u>Figure 1:</u> Methodology for developing an *ex vivo* system for micro-muscle contraction. A. Schematic representation of the method, combining photopatterning technique with culture of patient muscle cells (PDMS=Polydimethylsiloxane) (Created with BioRender.com). **B.** Transmitted light microscopic image of a chip's topography, and observation of a pillar duo at a higher magnification. **CDE.** Tilted scanning electronic microscopy images (30°) from few different pillar types. C: striations, D: pattern n°6 **(Supplementary table 2)**, E: pattern n°2 **(Supplementary table 2)**.

3.2. Matrigel coating micropatterning

To gain in 3D myotube density, micropillar duos were placed side by side on the chip without recessed wells to receive the seeded cells. We used LIMA technique **(Fig. 2A)** to avoid myoblast monolayer formation over the entire chip surface and restrict myoblasts adhesion in the inter-pillar area. This technique is based on the "passivation" of the substrate by PLL-PEG polymers. While the poly(L-lysine) backbone interacts electrostatically with the substrate, the poly(ethylene glycol) side chains block proteins

or cell adhesion (Strale et al., 2016). Combined to a photo-initiator, local exposure to UV degrades PLL-PEG, creating a region permissive to cell adhesion **(Fig. 2B)**.

The specificity of the Matrigel micropatterning was proved as cells would almost exclusively adhere to patterned areas from early proliferation phase to later stages of myotube maturation **(Fig. 2C)**. Diverse technical parameters were optimized, such as the UV exposure (the required minimal dose being 1000 mJ/mm^2 for optimal patterning) of PLL-PEG polymers **(Fig. 2D)**. The developed protocol enables to obtain Matrigel-coated areas exclusively between the pillar duos **(Fig. 2E)**, forcing the myoblasts to adhere in clusters and fuse into myotubes strictly in the axis of the pillars **(Fig. 2F)**.

Micropatterning-based clustering of cells appeared to be an essential element of culture success, since hydrogel embedment in both pure Matrigel or Matrigel/Collagen I mix, allowing branching between myotubes, displayed disastrous effects on 3D myotube culture yields **(Fig. S2)**, whereas controls on 2D monolayer cultures confirmed promotion of myotube maturation within Matrigel embedment **(Fig. S2A-E)** (Pimentel et al., 2017). The system was kept gel-free with only silicone substrate and liquid medium to support 3D myotube culture.

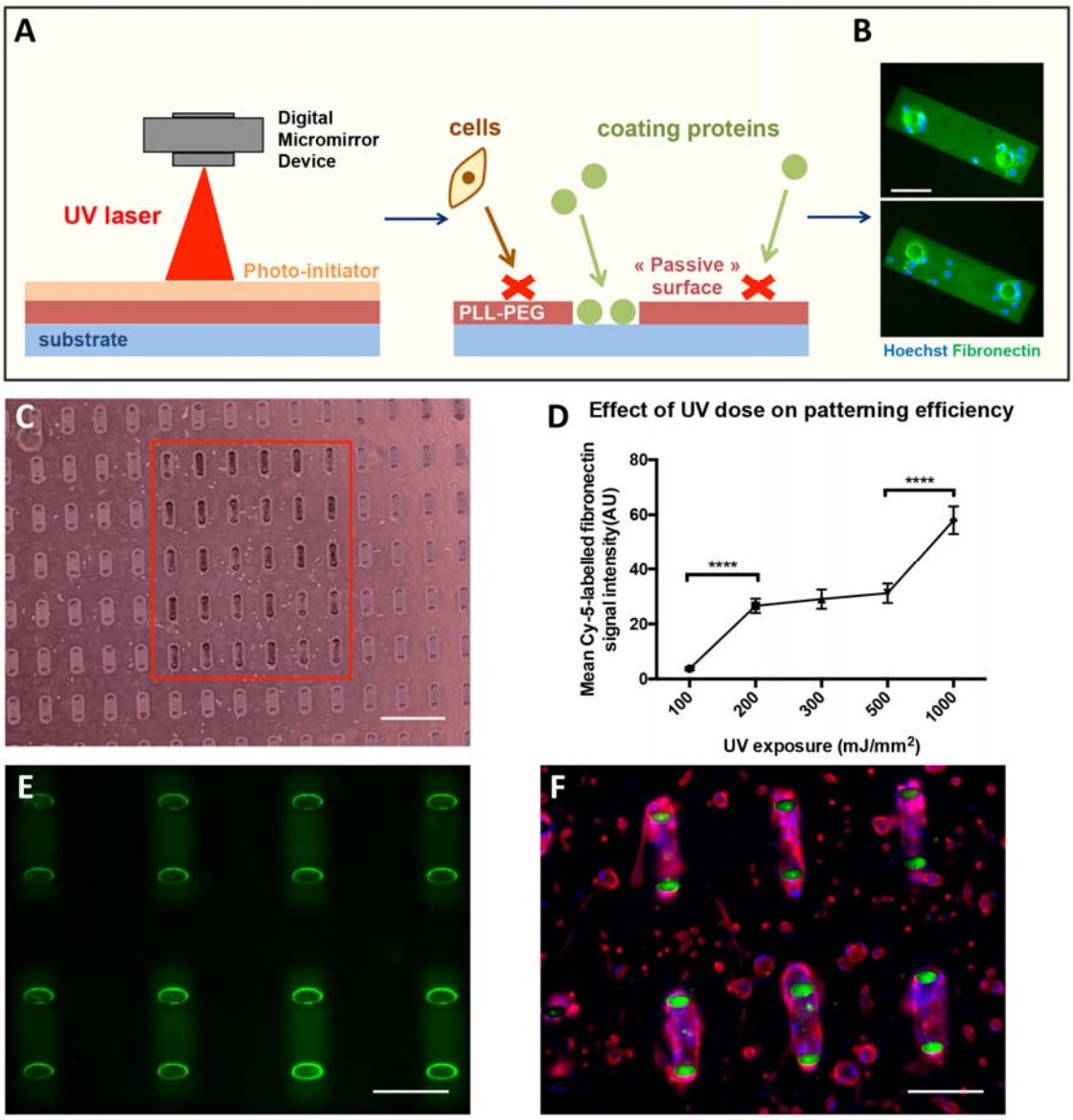

Figure 2: Micropatterning 3D myotubes with light induced molecular adsorption. A. Schematic representation of LIMA technique. **B.** Images of immunostained human immortalized fibroblasts nuclei (blue) plated on microsubstrates with Cy5-labeled fibronectin (green). Scale bar = 100 µm. **C.** Transmitted light microscopic image of 30 microtissues obtained from human immortalized (8220) myoblasts seeded the day before, forming within patterned area (red rectangle) (scale bar = 500 µm). **D.** Mean Cy-5 labelled fibronectin fluorescent signal intensity (± s.e.m.) measured after UV exposure along a spatial gradient. ****p<0.0001 (Unpaired t-test). **E.** Image of micropillars patterned with Fibronectin-Cy5/Matrigel mix (FN-Cy5 = green). Scale bar = 200 µm. **F.** Image of immunofluorescent staining of forming myotubes from human immortalized (8220) myoblasts after 7 days of differentiation on micropillars patterned with

FN-Cy5/Matrigel mix (Myosin heavy chain (red), FN-Cy5 (green), nuclei (blue). Scale bar = 200 µm.

3.3. Optimization of chip geometrical settings.

To facilitate myoblast alignment, 6 µm periodic striations, with a height of 3.5 µm, were sculpted in between the micropillar duos, as this pattern was already shown to produce the most healthy, aligned myoblasts when comparing to 3 and 12 µm periodicity size (Lam et al., 2006). This topographical modification drastically improved 3D myotube yield **(Fig. 3A-C)**. We only obtained a success rate of 6% for immortalized myoblasts-derived 3D myotube without striations whereas a 35% success rate on striated ones was achieved when collecting results from different pillar geometries **(Supplementary table 2**: patterns n°3, 4, 7 and 8, N=4 for each pattern**)**. This percentage was defined as the ratio of observed myotubes in between pillar duos after 7 days of differentiation over total number of prepared pillar duos. After fusion, the successfully formed myotubes embraced the pillars. Interestingly, we observed that during the maturation of the myotubes, their spontaneous contraction basically rips them of the surface inducing their lateral migration upward and leading to the bending of the two elastic pillars toward each other.

We then analyzed the impact of pillar geometry to determine the optimal conditions of myotube formation. The 3D myotube obtention rate decreased linearly with increasing pillar major axis **(Fig. S1)**. Two pillar shapes, presenting elliptic shapes with axial ratios close to 1.7 (**Supplementary table 2**: patterns n°5 and 6**)** provided optimized 3D myotube yields. After migration the microtissues remain suspended between these pillars at an average height of 75 µm (SD=11µm, N=30), independently of cell type as confirmed by observation on brightfield images and by scanning electron microscopy (SEM) **(Fig. 3D)**. Success rates reached respectively 80 %, for a major axis of 54 µm, and 58% for a major axis of 44 µm, after 7 days of differentiation, and 63 % and 58% after 10 days of differentiation **(Fig. 3E)**.

The pillar deflection can also be easily observed from the top by transmitted light microscopy, allowing to estimate the generated force, calculated from elastic beam with

ellipsoidal cross-section (Saez et al., 2007) **(Fig. 3F) (Supplementary table 2:** n°1, 2, 4, 5, 6**)**.

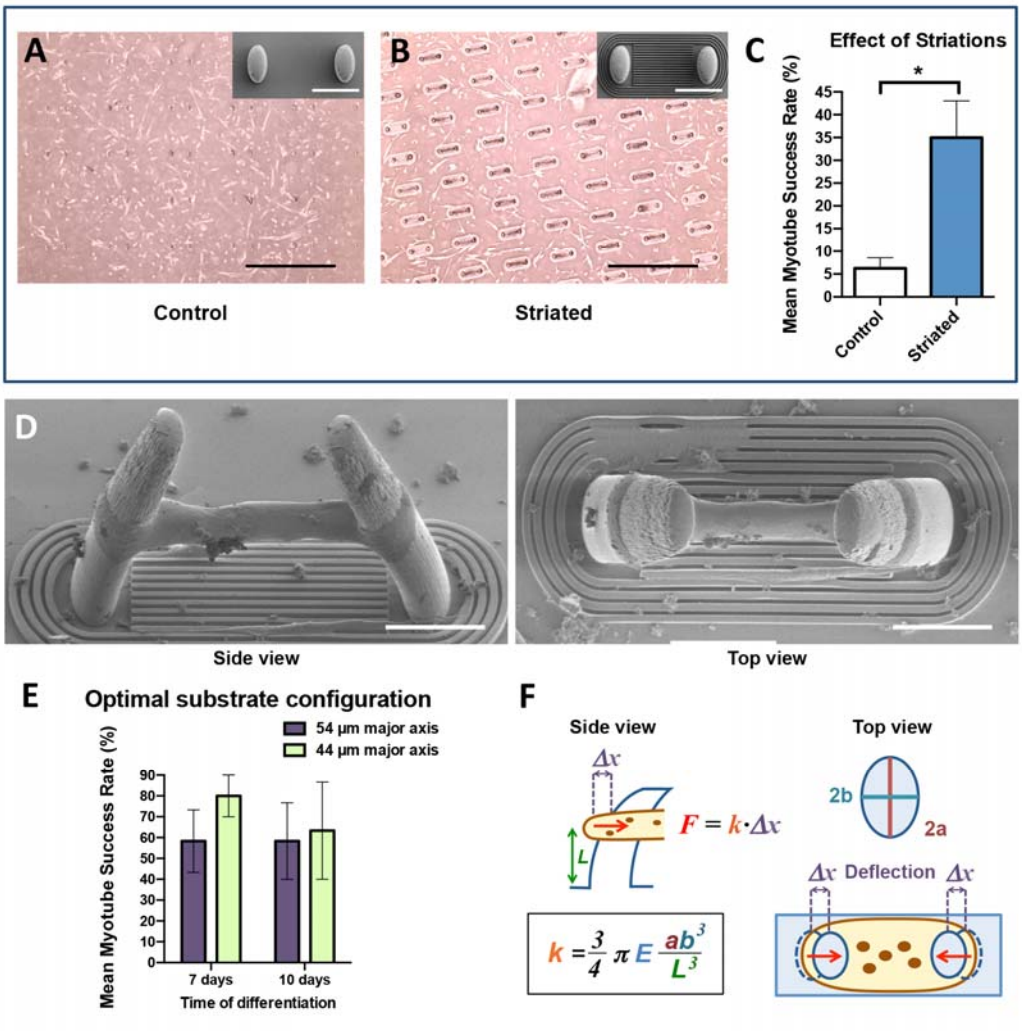

<u>Figure 3:</u> Optimization of substrate configuration for myotube culture efficiency. A,B. Transmitted light microscopic images of myotubes obtained from human immortalized myoblasts (8220 and AB1190) after 7 days of differentiation (scale bars = 100 µm), and associated scanning electronic microscopy images (scale bars = 600 µm) of corresponding non striated (B) and striated (C) identical micropillar duos (patterns n°7 and n°4 -**Supplementary table 2**). **C.** Analysis of mean 3D myotube culture success rate ± s.e.m. obtained from human immortalized (8220 and AB1190) myoblasts after 7 days of differentiation on patterned micropillars with or without 6 µm periodic striations (pillar n°3, n°4, n°7 and n°9 ; see **Supplementary table 2**). ± s.e.m. is represented, *p<0.05 (Wilcoxon matched-pairs signed rank test), N=4.. **D.** SEM images (top view and tilted view 45°) of a 3D myotube obtained from human immortalized (8220) myoblasts after 7 days of differentiation (pattern n°6 - **Supplementary table 2**). Scale bars = 50 µm. **E.** Analysis of mean myotube obtention success rate (± s.e.m.) from

human immortalized (8220 and AB1190) myoblasts after 7 and 10 days of differentiation on patterned micropillars with the two most optimal substrate configurations (pillar n°5 in purple and n°6 in green. See **Supplementary table 2**), N=2 (analysis was performed on at least 60 patterned pillar duos for each cell line). **F.** Calculation of the bending force per pillar with ellipsoidal cross-section (F: generated force; k: Spring constant (µN/µm) (Saez et al., 2007); E: PDMS 1:10 Young's modulus = 1.8 MPa ; 2a: major axis ; 2b: minor axis ; L: vertical position of the microtissue on the pillars).

3.4. Functional analysis of 3D myotubes.

Maturated 3D myotubes from primary human myoblasts cultured on micropillars successfully developed a sarcomeric network **(Fig. 4A)**, which spreads spatially in a cylindrical fashion **(Fig. 4B)**, according to the myotube shape, and expressing markers of the contractile apparatus (**Fig. 4C and 4D)** (e.g. titin and sarcomeric α-actinin respectively staining I-bands and Z-disks). The nuclei also aligned along the myotubes at different height levels **(Fig. 4E)**, similarly to myonuclei observed on isolated myofibers.

Following the formation of the contractile machinery, we observed input-free twitch contractions of our 3D myotubes **(Movie 1) (Supplementary Fig. S3)** (**Supplementary table 2**: pattern n°6), which could be monitored by pillar deflection tracking **(Fig. 4F-G**). Unlike most preceding models using optogenetic or electrophysiological activations (Afshar et al., 2020) (Mills et al., 2019), we observed spontaneous contraction events of the myotubes after myofibril expression has been reached. Spontaneous contractions were recorded on primary **(Fig. 4F) (Movie 1)** and immortalized **(Fig. 4G) (Movie 2)** myoblasts-derived 3D myotubes (with respectively 44 and 183 monitored contractions phenomena). Primary myoblasts-derived 3D myotubes systematically displayed a repetitive and stereotyped pattern of contractions within approximately 1.5 second, with a stability of the force value normalized by the number of nuclei for each myotube **(Fig. 4H)**, notably the value corresponding to the peak **(Fig. 4I)**. We first observed a fast increase of the force until the peak of the contraction (after 0.5 second), followed by a progressive force decrease (lasting 0.5 to 1 second). Immortalized myoblasts-derived 3D

myotubes displayed a similar pattern of contraction, but with a reduced intensity (1.14 +/- 0.04 µN instead of 2.44 +/- 0.06 µN) in a reduced time frame (0.43 +/- 0.01 second instead of 1.03 +/- 0.03 second) **(Fig. 4H-I)**. The frequency is four times superior, with values respectively of 1.11 Hz for the immortalized myoblasts **(Fig. 4G)** and 0.27 Hz for the primary myoblasts **(Fig. 4F)**. Furthermore immortalized myoblasts-derived 3D myotubes displayed a strong variability of spontaneous contraction intensity in comparison to primary myoblasts-derived 3D myotubes (with respectively 44.77% and 9.28% variation coefficients).

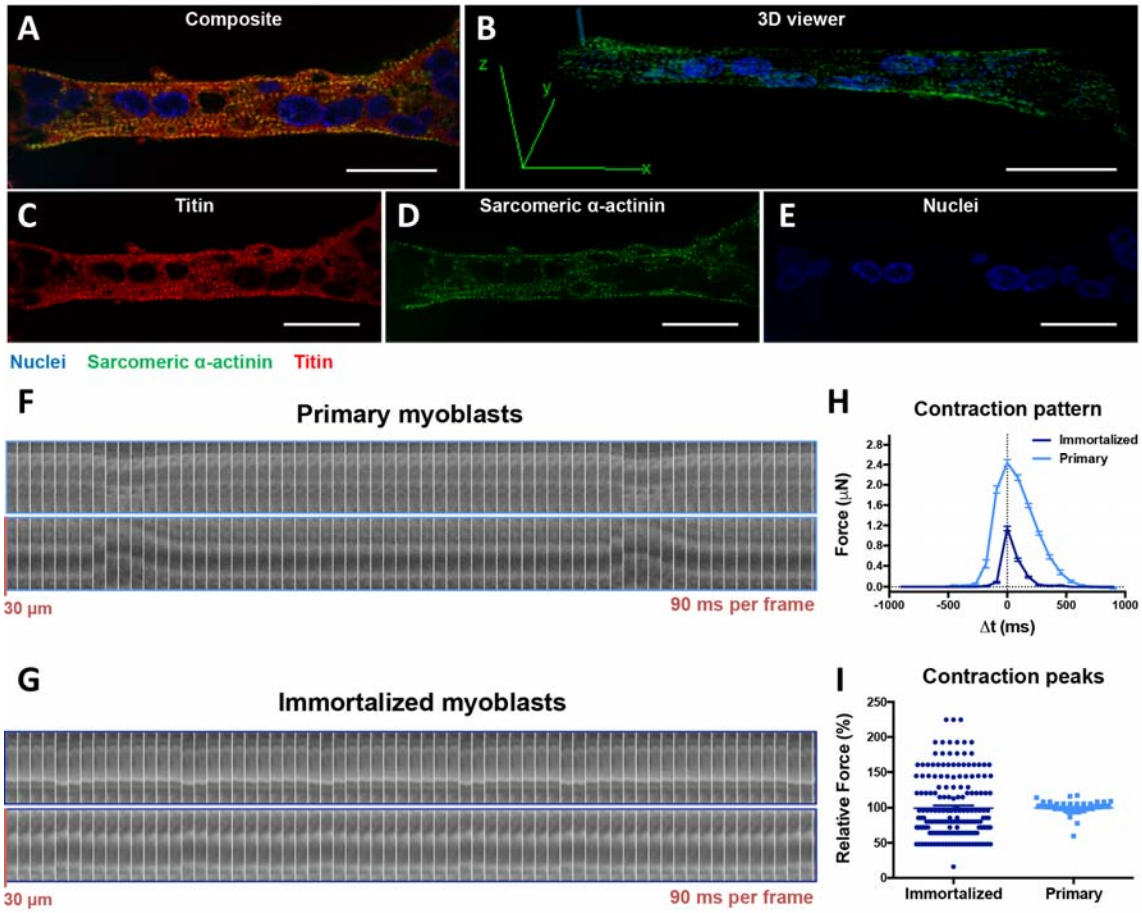

<u>Figure 4:</u> Monitoring of spontaneous contraction generated by mature 3D myotubes. A,B,C,D,E. Representative images of immunofluorescent stained 3D myotubes obtained from human primary (AB678C53Q) myoblasts after 12 days of differentiation (Sarcomeric α-actinin (green), Hoechst (blue), Titin (red), scale bars = 25 µm) as a confocal section (A,C,D,E) and a three-dimensional view (B). **F,G.** Transmitted light kymographs of pillar deflections over time with 3D myotubes from primary (AB678C53Q) (F) and immortalized (8220) (G) myoblasts after

9 days of differentiation. **H.** Mean relative contraction force over time (Normalized with nuclei number: Each force was multiplied by this nuclei ratio = (100 / nuclei number) to be standardized based on a 100 nuclei tissue; considered height: 75 µm) ± s.e.m. generated by 3D myotubes from human primary (AB678C53Q) (light blue) and immortalized (8220) (dark blue) myoblasts after 9 days of differentiation. (pillar n°6. See **Supplementary table 2**) (primary: N=2; 44 contractions (dots) observed, immortalized: N=3; 183 contractions (dots) observed). **I.** Relative forces of contraction peaks (normalized with mean peak contraction force) ± s.e.m. generated by 3D myotubes from human primary (AB678C53Q) (light blue) and immortalized (8220) (dark blue) myoblasts after 9 days of differentiation (primary: N=2; 44 contractions (dots) observed, immortalized: N=3; 183 contractions (dots) observed).

3.5. Morphological impact of 3D culture on myonuclei.

Muscle disorders such as laminopathies are known to affect myonuclei structure, which have also been found to display variation in shape when cultured in 3D rather than 2D in previous skeletal muscle organoids (Maffioletti et al., 2018). To investigate the morphological impact of 3D culture on nuclei shape in comparison to 2D culture, we analyzed the 3D myotube organization at different length scale. We measured each nucleus projection area slice by slice on a vertical z axis, as well as their 3D features **(Fig. 5A-D)**. Representation of mean normalized area (with regard to Maximal Slice Area – MSA) as a function of the distance from the nucleus center gives an indication of the 3D shape, with steeper slopes corresponding to flatter nuclei. The distributions of nuclei slice areas showed that nuclei within 3D myotubes presented largely reduced flatness compared to nuclei from 2D monolayers **(Fig. 5E)**. However, nuclei from 3D myotubes conserved a similar ellipticity **(Fig. 5F)**, showing that the nuclear width and length evolved in the same proportions. In comparison to nuclei from 2D monolayers, nuclei from 3D myotubes had heights twice superior (respectively 3.2 µm and 7 µm) **(Fig. 5G)**. In addition, 3D nuclei also exhibited decreased volume **(Fig. 5H)** compared to 2D nuclei (respectively 229 μm^3 and 285 μm^3).

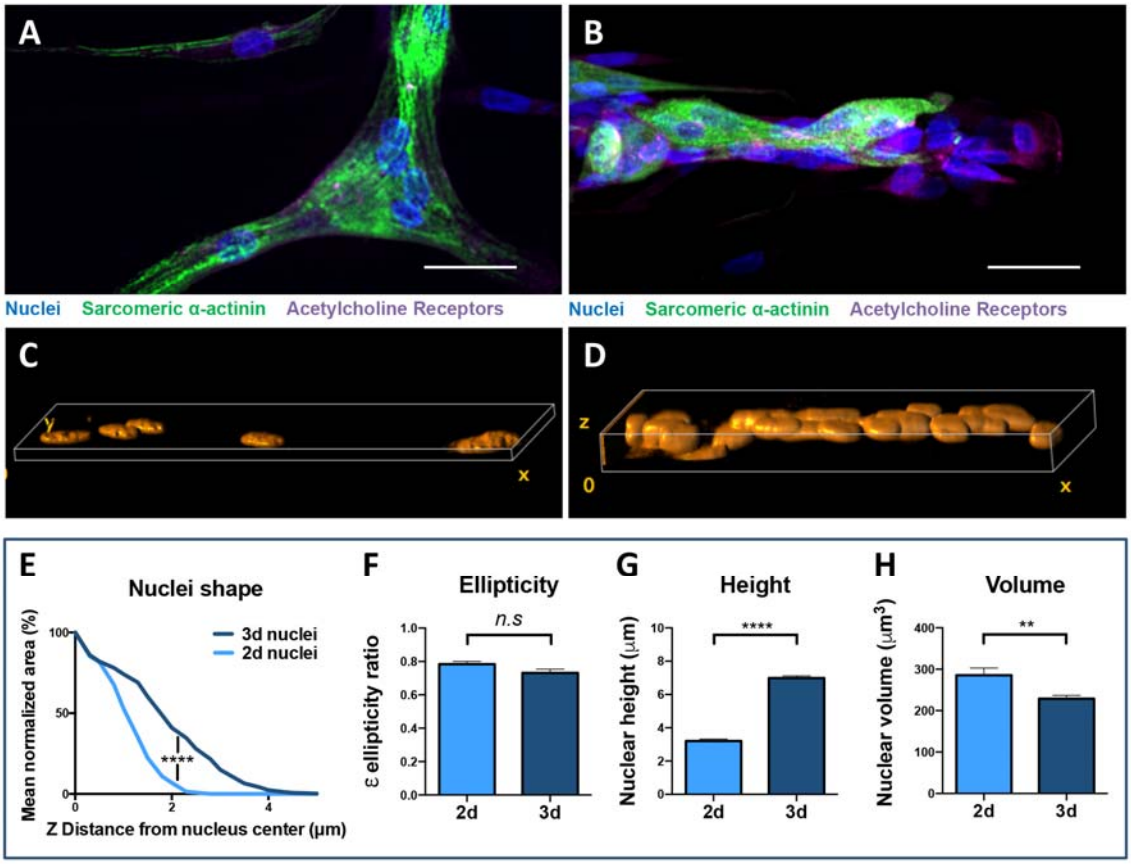

Figure 5: Shape and dimensions of nuclei within 2D monolayer and 3D myotubes. A,B. Representative (top view) images of an immunofluorescent stained monolayer of myotube (A) and 3D myotube (B) obtained from human primary (AB678C53Q) myoblasts after 7 days of differentiation (Sarcomeric α-actinin (green), Hoechst (blue), Acetylcholine receptors (magenta) scale bars = 25 µm). **C,D.** Volume viewer of Hoechst-stained nuclei from tilted representative images of myotubes monolayer (C) and 3D myotube (D) obtained from human primary myoblasts after 7 days of differentiation (rotations : x=105 ; y=15 ; x=0). **E.** Distributions of mean normalized areas calculated in 2D myotubes monolayers and 3D myotubes obtained from human primary (AB678C53Q) myoblasts after 7 days of differentiation. ****$p<0.0001$ (Wilcoxon matched-pairs signed rank test), 2D = 35 nuclei; 3D = 69 nuclei. **F.** Mean nuclear (xy) ellipticity ± s.e.m. in 2D myotubes monolayer and 3D myotubes obtained from human primary myoblasts after 7 days of differentiation. *n.s* not significant (Mann-Whitney unpaired test), 2D = 35 nuclei;

3D = 69 nuclei. **G.** Mean nuclear height ± s.e.m. in 2D myotubes monolayer and 3D myotubes obtained from human primary myoblasts after 7 days of differentiation. ****$p<0.0001$ (Unpaired *t*-test), 2D = 35 nuclei; 3D = 69 nuclei. **H.** Mean nuclear volume (± s.e.m.) in 2D myotubes monolayer and 3D myotubes obtained from human primary myoblasts after 7 days of differentiation. **$p<0.01$ (Mann-Whitney unpaired test), 2D = 35 nuclei; 3D = 69 nuclei. (pillar n°6. See **Supplementary table 2**)

3.6. Expression of pathological nuclear phenotypes in patient 3D myotubes.

We then used our device to investigate the mechanical differences between 3D myotubes from healthy **(Fig. 6A)** and L-CMD **(Fig. 6B)** patients immortalized myoblasts. As observed in 3D reconstitutions from confocal imaging **(Fig. 6C-D)**, nuclei with *LMNA* mutation displayed morphological differences compared to control nuclei. First, *LMNA* mutation was associated to a significant increase of nuclear flatness **(Fig. 6E-F)**, in comparison to control nuclei. Furthermore, while maintaining a constant nuclear ellipticity **(Fig. 6G)**, 3D myotubes issued from L-CMD patients also differed from control myotubes by presenting longer (respectively 14.5 µm and 11.4 µm) and wider (respectively 9.6 µm and 7.1 µm) nuclei (**Fig.6H-I**). Confirming the relative flatness of LMNA mutated nuclei, the height **(Fig. 6J)** was slightly but significantly reduced compared to control nuclei (respectively 5.2 µm and 5.8 µm), despite the larger volume **(Fig. 6K)** of mutant nuclei (211 μm^3 against 162 μm^3 in control nuclei). Altogether, these results showed that once put in our system, patient-derived myoblasts can generate 3D myotube reproducing typical L-CMD pathological phenotype which have previously been reported (Bertrand et al., 2014)(Maffioletti et al., 2018).

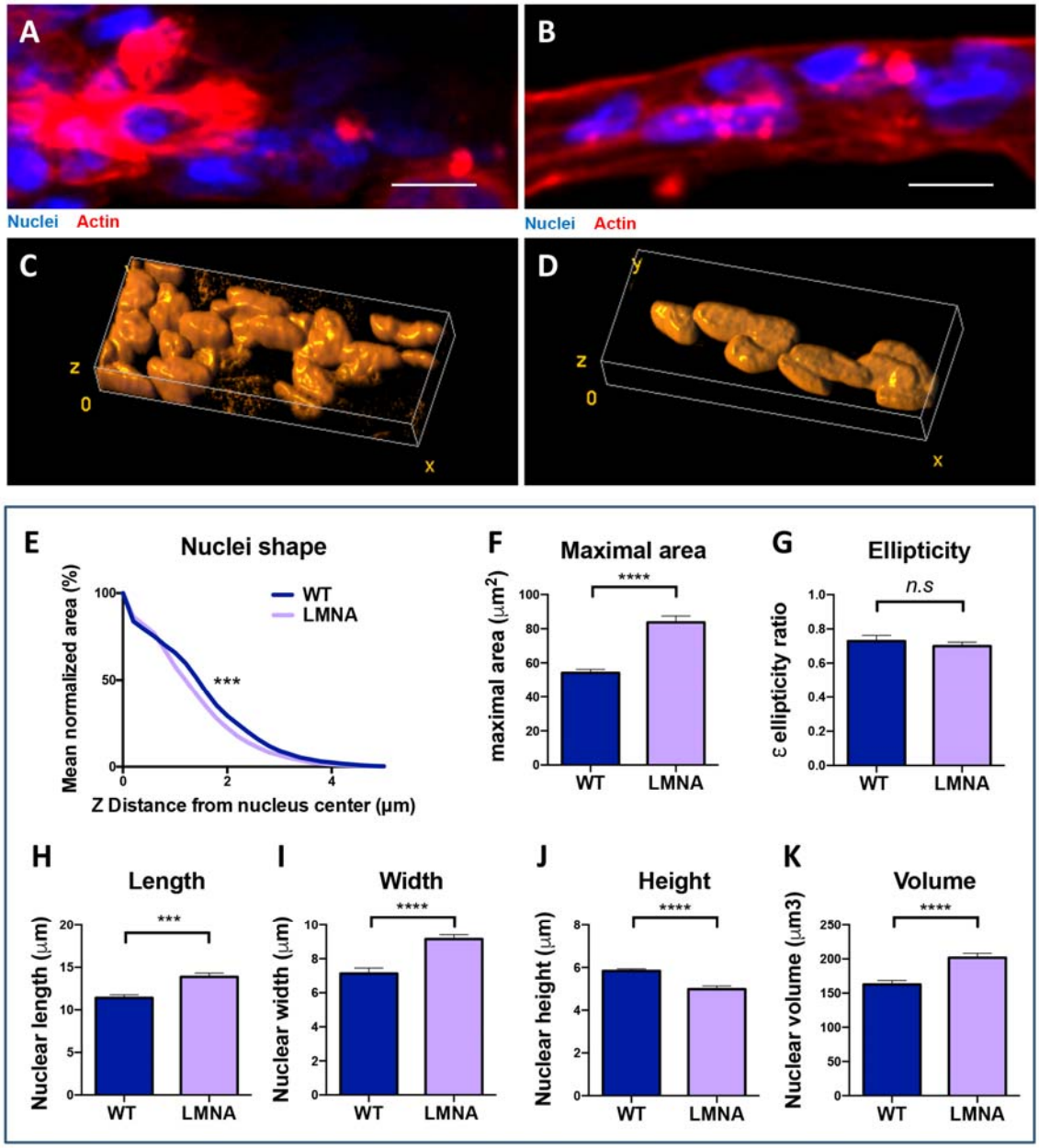

<u>Figure 6:</u> Effect of a LMNA gene mutation on nuclei morphology in patient 3D myotubes. **A,B.** Representative (top view) images of immunofluorescent stained 3D myotubes obtained from control (A) and L-CMD (B) patients myoblasts (respectively 8220 and EMD1365) after 7 days of differentiation (Hoechst (blue), phalloidin (red) scale bars = 25 µm, both images are later analyzed in C and D). **C,D.** Volume viewer of Hoechst-stained nuclei from tilted representative images of 3D myotubes from control (C) and L-CMD (D) patients myoblasts after 7 days of differentiation (rotations : x=150 ; y=15 ; x=10). **E.** Distributions of mean normalized areas calculated in 3D myotubes from control (8220) and L-CMD (EMD1365) patients' myoblasts after 7 days of differentiation. ***p<0.001 (Wilcoxon matched-pairs signed rank test), WT = 57 nuclei;

LMNA = 85 nuclei. **F.** Mean area at the central slice of the nuclei ± s.e.m. ****p<0.0001 (Mann-Whitney unpaired test). **G.** Mean nuclear (xy) ellipticity ± s.e.m. in 3D myotubes from control (8220) and L-CMD (EMD1365) patients' myoblasts after 7 days of differentiation. *n.s* not significant (Unpaired *t* test), WT = 57 nuclei; LMNA = 85 nuclei. **H,I,J,K.** Mean nuclear length (H), width (I), height (J) and volume (K) ± s.e.m. in 3D myotubes from control (8220) and L-CMD (EMD1365) patients myoblasts after 7 days of differentiation. ***p<0.001; ****p<0.0001 (Mann-Whitney unpaired test), WT = 57 nuclei; LMNA = 85 nuclei. (pillar n°6. See **Supplementary table 2**).

3.7. Contractile dysfunction in L-CMD patients 3D myotubes.

To assess the functional features of pathological constructs, we monitored pillar deflections caused by the contractile activity of 3D myotubes issued from healthy donors **(Fig. 7A)** (Movie 2) and L-CMD patients **(Fig. 7B)** (Movie 3) immortalized myoblasts. We observed smaller deflections of the pillars in 3D myotubes carrying *LMNA* mutation **(Fig. 7C)** as compared to control myotubes. Unlike in control myotubes, spontaneous twitch contractions could not be observed in *LMNA* mutant myotubes. These amplitudes were also both significantly higher in comparison to inactivated 3D myotubes (pre-treated with 20 µM Acetylcholine) **(Fig. 7C)**. Moreover, the difference in absolute pillar deflection amplitude could not be observed when normalized with nuclei number **(Fig. 7D)**. Indeed, LMNA mutant myotubes contained less nuclei than the control myotubes (with respective means of 62.7 and 80.0 nuclei per myotube, data not shown). This suggests that these lower amplitudes and associated weaker forces are related to a reduction in the efficiency of muscle cell fusion and subsequent myotube formation in LNMA-mutant context.

In conclusion, the micro-muscle chip developed here can accurately measure differences in force generation by constructs generated from muscle cells expanded from patients with genetic muscular diseases.

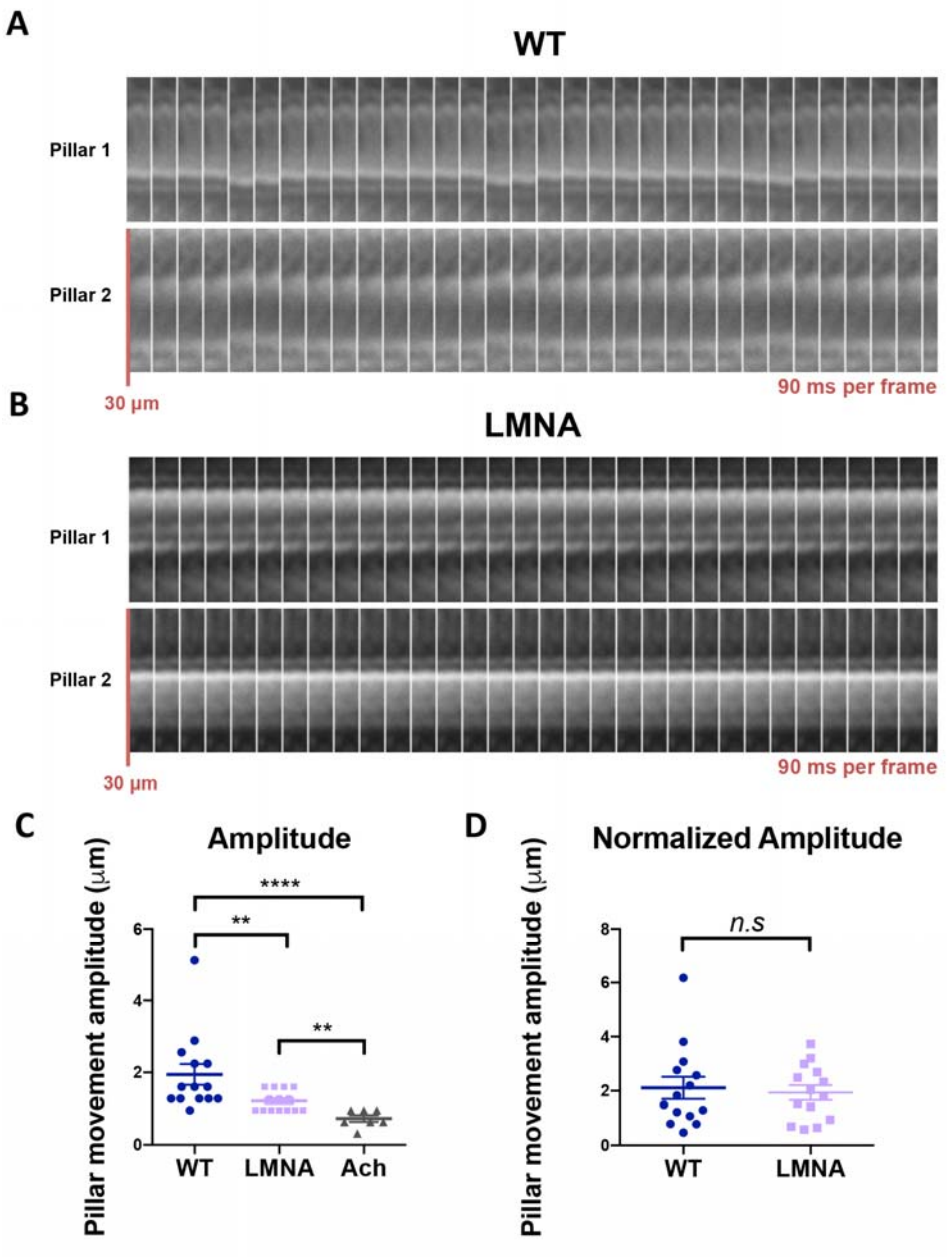

<u>Figure 7:</u> Effect of a LMNA gene mutation on contractile activity of 3D myotubes obtained from patients' myoblasts. A,B. Transmitted light kymographs of pillars deflection over time with 3D myotubes from control (8220) (A) and L-CMD (EMD1365) (B) patients immortalized myoblasts after 9 days of differentiation. **C.** Mean maximal amplitude of movement ± s.e.m. (measured on 9 seconds films) of pillars with 3D myotubes from control (8220) or L-CMD (EMD1365) patients' myoblasts and 3D myotubes inactivated with 20 µM Acetylcholine, after 9 days of differentiation. **p<0.01; ****p<0.0001 (Mann-Whitney unpaired test), N=14 (and 7 Acetylcholine-inactivated myotubes). **D.** Mean maximal amplitude of movement (Normalized with nuclei number: Each force was multiplied by this nuclei ratio = (70 / nuclei number) to be

standardized based on a 70 nuclei tissue) ± s.e.m. (measured on 9 seconds films) of pillars with 3D myotubes from control (8220) and L-CMD (EMD1365) patients' myoblasts after 9 days of differentiation. *n.s* = not significant (Mann-Whitney unpaired test), N=14.

4. Discussion

We developed a tissue-on-chip culture device allowing the assessment of forces generated by 3D myotubes from healthy donors or from patients suffering muscular disorders. The system relies on a combination of optimized geometrical features of the substrate, namely pillar duos linked together by micropatterned linear striations, with adhesive proteins micropatterning mediated by light-induced molecular adsorption. Fine tuning of each parameter contributes to increasing skeletal muscle organoids yield, and the underlying principles allow for further downsizing of the system. Thereby, this technology offers perspectives for implementation in myology research and organ-on-chip bioengineering for medical studies. This model might offer less versatility than other muscle constructs (Maffioletti et al., 2018) (Afshar et al., 2020) (Osaki et al., 2020), which recreate muscle-like beams of fiber bundles, and allow co-culture of vascular (Maffioletti et al., 2018) and neuronal (Afshar et al., 2020) (Osaki et al., 2020) tissues. Also, the presence of residual myocytes between patterned areas **(Fig. 2F)** could eventually bias bulk RNA and protein based molecular biology approaches performed with other models (Rao et al., 2018) (Mills et al., 2019). However, we propose a culture device with an unprecedented cells-to-construct ratio designed to produce a great number of technical replicates with relatively few cells. Each 3D myotube requires 1 000 to 6 667 seeded myoblasts (considering that 100k cells are plated to obtain 100 myotube/chip in optimal conditions, whereas 200k cells are plated to obtain 30 myotube/chip in the worst conditions, such as the most severe mutant phenotype), depending on the cell type (in particular, primary or immortalized, control or mutant, etc…). For comparison purposes, 3D Artificial Muscles (Maffioletti et al., 2018) requires one million of cells per construct ($x10^3$ more), MyoTACTIC (Afshar et al., 2020) uses gel suspension with 15 millions cell/mL, NMJ chip (Osaki et al., 2020) have an estimated biological cost of 84 000 cells per tissue and human skeletal micro muscles (Mills et al., 2019) need 30 000 cells per tissue ($x10^1$ more). Downsizing of the system could still be optimized by increasing pillar density to maximize 3D myotube culture yield.

The system has been optimized with diverse cell lines, primary or immortalized myoblasts, obtained from different muscle groups and from various patients with diverging ages and phenotypes **(Supplementary table 1)**. 3D myotubes were obtained

for the two healthy myogenic immortalized lines. There is a strong reproducibility between experiments performed with the same cell line, which ensures the reliability of this platform when used to study the effect of a therapeutical drug on a patient cell line. Nevertheless, there is an unequal yield (increasing with duration of culture) depending on the cell line (data not shown), most likely due to uneven adhesion capacity, passive resting tension and sarcomere-generated contraction forces. Consequently, the chip configuration should ideally be fine-tuned for each myogenic lineage, in particular to control the physical parameters such as the stiffness constraints applied to the myotubes. In the present study 3D myotube culture was optimal using the two elliptic pillar shapes presenting the lowest major axis values **(Fig. 3E)**. Counterintuitively, the tissue stability decreased linearly with increasing pillar major axis **(Fig. S1)**, suggesting that higher adhesion surfaces did not prevent myotube detachment. On the contrary, the wider myotubes seem to detach more easily, possibly due to increased contractile material.

Addition of round caps or internal bending of pillar top is widely spread in other muscle culture models (Osaki et al., 2020) (Afshar et al., 2020) in order to increase anchoring of the microtissues onto the pillars. Most 3D skeletal muscle *in vitro* models are indeed borne by gel-based scaffolds providing a structural support for cells to fuse and spread in all three spatial dimensions. The hosting matrix can be composed of various ECM components to imitate the microenvironment, such as fibrin gels (Chiron et al., 2012), fibronectin-gelatin nanofilms (Gribova et al., 2016), and most interestingly collagen-matrigel mix (Mills et al., 2019). The gel suspension is also thought to provide the proliferating cells with a condition closer to the *in vivo* environment of early skeletal muscle regeneration, in terms of chemical interactions with the ECM proteins and the physical constraints mimicking a necrosed myofiber. Our system does not require the use of a hydrogel scaffold and rather relies on the production by the cells of their own matrix along the tissular formation process. Upward migration along the pillars is induced by spontaneous contraction of the tissues. Abstaining from any preexisting hydrogel allows proper pre-alignment of the seeded myoblasts in the substrate micropatterned striations, which is a major factor to ensure success of myotube formation and enables to induce mono-cylindrical shaping of the sarcomeric network. The formed myotube bundles are more compact with straighter orientation. Indeed, the

alignment along the axis joining the pillars takes place in a steadier manner than in models using gel scaffolds (Sakar et al., 2012) (Cvetkovic et al., 2014) (Mills et al., 2019). This is beneficial since variability in myotube density and orientation within the gel construct might create biases of force measurement.

Spontaneous twitch contractions in 3D myotubes derived from human myoblasts were observed with a high degree of reproducibility, highlighting the relevance of this technology. Contractions of primary tissues obtained with other reported protocols are induced by optogenetic (Mills et al., 2019)(Afshar et al., 2020) or electrophysiological (Rao et al., 2018) stimulations. The observation of spontaneous contractions in our system highlights its relevance to study contractions in a clinical setting, as cells can be used directly from the patient' biopsies. Still, spontaneous contractions were not systematically observed in every matured tissue. Use of specific drugs (Caffein, Calmodulin, Nocodazol, Rapamycin, Bosutinib, Reparixin, etc…), ions (Calcium, Potassium, etc…), and other molecular supports such as ATP (Osaki et al., 2020) that are known to induce contractions, could be used to increase steadiness of obtained results. spontaneous contractions were also observed in immortalized myoblasts-derived 3D myotubes **(Fig. 4)** and presented different contraction characteristics when compared to primary myoblasts-derived 3D myotubes. The observed reduced and more frequent contractions could be explained by desynchronized activation of the different myofibrils within the 3D myotubes, leading to a fibrillatory pattern. Contractions generated by immortalized myoblasts-derived 3D myotubes also displayed important variability **(Fig. 4I)**, which seems to indicate a higher relevance of the system for primary myoblasts contraction analysis in comparison to immortalized cells, and further highlights the interest of this miniaturized culture system to harness patients' biopsies.

The specific forces of the spontaneous contractions here observed are in the order of few mN/mm^2, which is comparable to the specific forces of twitch and tetanic contractions measured in other muscle microtissues (Afshar et al., 2020) (Rao et al., 2018) (Mills et al., 2019) (Sakar et al., 2012). This value is particularly interesting due to the spontaneous nature of the observed contractions, as opposed to the activated contractions reported in the literature.

Our reduced-scale model allows to precisely image subcellular structure like nuclei, sarcomeric network and many others. As expected, in absence of direct physical constraints from the substrate, 3D myotube nuclei substantially lost their 2D flatness **(Fig. 5)**. The nuclei kept a length superior to their width and height, which is most likely due to the longitudinal mechanical forces exerted within the myotube by the cytoskeleton. This nuclear phenotype could also be reproduced previously by exerting external force on gel-borne nuclei (Bertrand et al., 2014). The overall volume of 2D monolayer nuclei was found to be more important than the one of 3D myotube, confirming the relative morphological aberrance caused by 2D culture and proving the need for three-dimensional systems of culture. The shape of 3D myotube nuclei is closer to the in vivo conformation of myonuclei (Bruusgaard et al., 2010)(Hastings et al., 2020), which makes our culture chip a relevant tool for the analysis of nuclei-linked pathology, such as laminopathies.

The importance of the lamin envelope for nuclei morphological integrity is well known (Sullivan et al. 1999). Mutations in *LMNA* gene, encoding Lamin A and Lamin C proteins, are leading to striated muscle laminopathies, among which L-CMD, is the most severe type (Bertrand et al., 2020). The mutated lamins A/C are causing nuclear defects such as chromatin protrusion and nuclear envelope rupture (Earle et al., 2020). The ΔK32-P1 mutant myoblast lineage (Bertrand et al., 2014) we cultured into 3D myotube expressed the same phenotype that has been previously observed in preceding 3D skeletal muscle platforms (Maffioletti et al., 2018). *LMNA* mutated nuclei showed similar morphological aberrations such as increased flatness and volume. This proves that our 3D myotube culture chip is a reliable system to model morphological abnormalities of muscular disorders. In addition, *LMNA* mutant 3D myotube displayed reduced absolute contractile activities compared to control 3D myotubes **(Fig. 7C)**. However, this difference could not be observed after normalization with the tissue size, assessed based on total nuclei number, suggesting that this contractile dysfunction is due to abnormal tissue formation and could be solved by improving early myogenesis of LMNA mutant tissue. We anticipate that our device can thus be implemented as a readout for therapeutic drug screening for myopathies.

Acknowledgements:

The authors would like to thank Sylvie Hénon and Vincent Gache for fruitful discussion. Joseph d'Alessandro and Lakhmi Balasubramaniam are kindly acknowledged for their help with substrate preparation. The authors thank David Montero and the Institut des Matériaux de Paris Centre (IMPC FR2482) for servicing FEGSEM & EDX instrumentation. Cell lines were obtained thanks to the Myoline platform from the Institut de Myologie, Paris and to the Biobank support of the London MRC Neuromuscular Translational Research Centre and the Biomedical Research Centre of Great Ormond Street Hospital for Children in London. This work was supported by grants from the Agence Nationale de la Recherche (ANR-19-CE13-0016 MyoFuse), the Mechanobiology Institute (to G.G.), the LabEx "Who Am I?" #ANR-11-LABX-0071, the Université de Paris IdEx #ANR-18-IDEX-0001, the AFM/Téléthon and C'Nano program of the Région Ile-de-France. N.R. was supported by a French Ministère de la Recherche fellowship, Interfaces pour le vivant doctoral program from Sorbonne Université.

Supplementary data

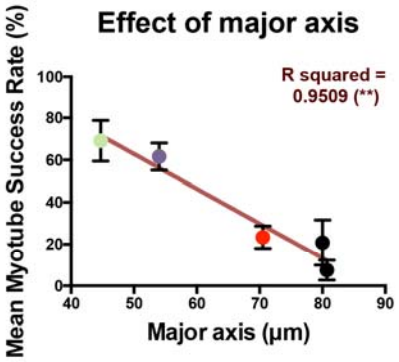

<u>Figure S1:</u> Effect of pillar major axis on culture yield. Analysis of 3D myotube obtention success rate ± s.e.m. obtained from human immortalized (8220 and AB1190) myoblasts after 7 days of differentiation on patterned micropillars with various major axis (pillar n°1, 2, 4, 5, 6 with 140 µm and 190 µm approximate interpillar distance. See **Supplementary table 2**). Linear regression (red line) and Pearson correlation test (**p<0.01) and coefficient (R squared = 0.9509), N=4.

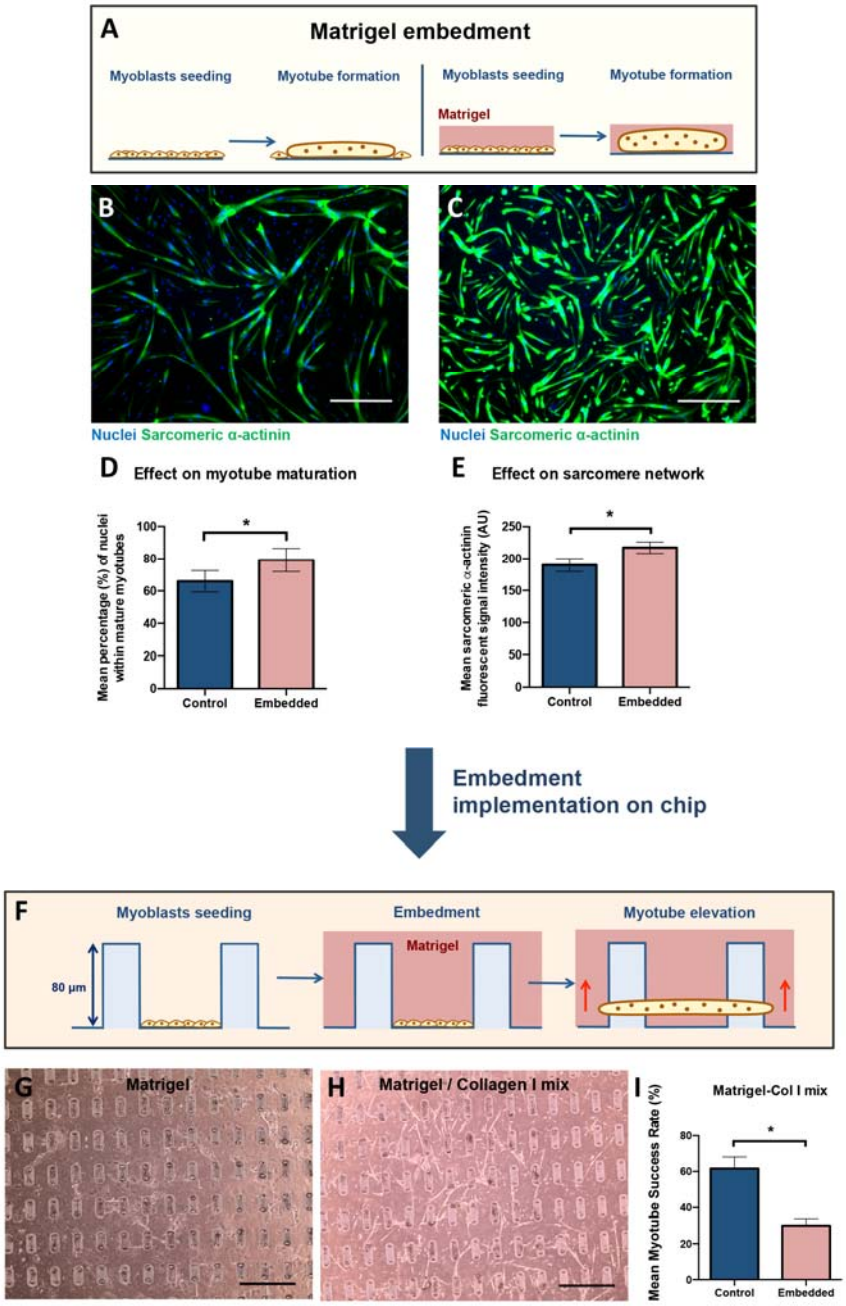

Figure S2: Incrementation of gel embedment methods in the system. A. Schematic representation of Matrigel embedment protocol (right) in comparison to classic 2D culture of myotubes (left). **B,C.** Representative images of immunofluorescent stained myotubes (from human immortalized myoblasts) after 6 days differentiation in normal 2D culture conditions (B) and Matrigel embedment conditions (C) (Sarcomeric α-actinin (green), nuclei (blue) scale bars = 500 µm). **D.** Mean percentage ± s.e.m. of nuclei located within mature (Sarcomeric α-actinin-expressing) myotubes (from human immortalized (8220 and AB1190) myoblasts) after 6 days of differentiation with or without Matrigel embedment. *p<0.05 (Wilcoxon matched-pairs signed

rank test), N=3. **E.** Mean fluorescent signal intensity (Arbitrary Unit) ± s.e.m. from labeled Sarcomeric α-actinin of myotubes (from human immortalized (8220 and AB1190) myoblasts) after 6 days of differentiation with or without Matrigel embedment. *$p<0.05$ (Wilcoxon matched-pairs signed rank test), N=3. **F.** Schematic representation of Matrigel embedment protocol adapted to 3D myotube culture on chip. **G,H.** Transmitted light microscopic images of myotubes (from human immortalized (8220 and AB1190) myoblasts) after 7 days of differentiation with pure Matrigel (G), and Matrigel/Collagen I mix (H) embedments. Scale bars = 500 µm. **I.** Mean myotube culture success rate ± s.e.m. obtained from human immortalized (8220 and AB1190) myoblasts after 7 days of differentiation on chip in normal culture conditions or Matrigel/Collagen I mix embedment. *$p<0.05$ (Mann-Whitney unpaired test), N=4.

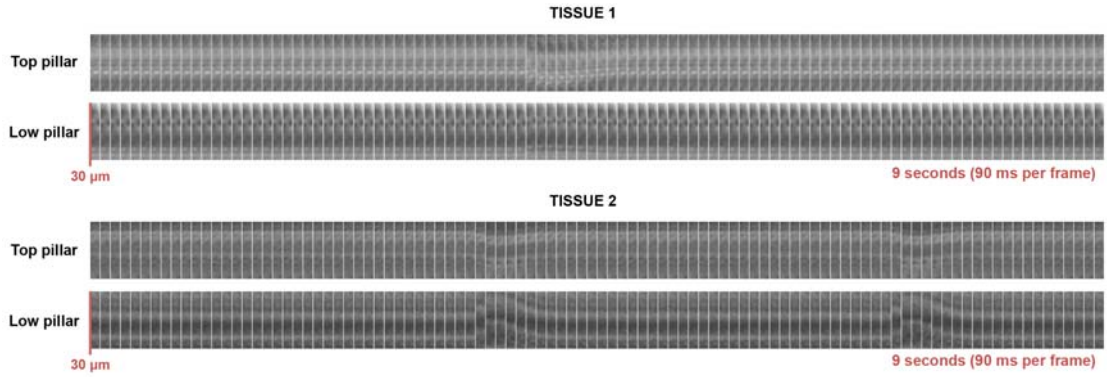

Figure S3: Kymographs. Transmitted light microscopic images of contracting 3D myotubes from human primary (AB678C53Q) myoblasts after 9 days of differentiation.

Cell Line	Genotype	Phenotype	Lineage	Muscle	Sex	Age
8220	-	Healthy	Immortalized	Paraspinal	Male	12 yo
AB1190	-	Healthy	Immortalized	Paravertebral	Male	16 yo
EMD1365	LMNA AAG, pLys32del c. del94-96	LMNA related Congenital Muscular Dystrophy	Immortalized	Right gluteal	Male	13 yo
AB678C53Q	-	Healthy	Primary	Quadriceps	Male	53 yo

Supplementary table 1: Description table of cell lineages used in the presented figures.

Pattern n°	Striation	Shape	Minor axis (µm)	Major axis (µm)	Axial ratio	Height (µm)
1	3.5 µm	Ellipse	57	80.7	1.4	148.5
2	3.5 µm	Ellipse	21.4	70.5	3.3	137
3	3.5 µm	round	57	-	1	138
4	3.5 µm	Ellipse	44	80	1.8	145
5	3.5 µm	Ellipse	30	54	1.8	130
6	3.5 µm	Ellipse	27	44.7	1.7	135
7	None	Ellipse	42.4	81.5	1.9	145
8	None	Ellipse	57	-	1	

Supplementary table 2: Description table of PDMS microfabricated pillar patterns used in the presented figures.

References

Afshar, M.E., Abraha, H.Y., Bakooshli, M.A., Davoudi, S., Thavandiran, N., Tung, K., Ahn, H., Ginsberg, H.J., Zandstra, P.W., and Gilbert, P.M. (2020). A 96-well culture platform enables longitudinal analyses of engineered human skeletal muscle microtissue strength. Sci Rep *10*, 6918.

Balaban, N.Q., Schwarz, U.S., Riveline, D., Goichberg, P., Tzur, G., Sabanay, I., Mahalu, D., Safran, S., Bershadsky, A., Addadi, L., et al. (2001). Force and focal adhesion assembly: a close relationship studied using elastic micropatterned substrates. Nat Cell Biol *3*, 466–472.

Bertrand, A.T., Ziaei, S., Ehret, C., Duchemin, H., Mamchaoui, K., Bigot, A., Mayer, M., Quijano-Roy, S., Desguerre, I., Laine, J., et al. (2014). Cellular microenvironments reveal defective mechanosensing responses and elevated YAP signaling in LMNA-mutated muscle precursors. Journal of Cell Science *127*, 2873–2884.

Bertrand, A.T., Brull, A., Azibani, F., Benarroch, L., Chikhaoui, K., Stewart, C.L., Medalia, O., Ben Yaou, R., and Bonne, G. (2020). Lamin A/C Assembly Defects in LMNA-Congenital Muscular Dystrophy Is Responsible for the Increased Severity of the Disease Compared with Emery–Dreifuss Muscular Dystrophy. Cells *9*, 844.

Boudou, T., Legant, W.R., Mu, A., Borochin, M.A., Thavandiran, N., Radisic, M., Zandstra, P.W., Epstein, J.A., Margulies, K.B., and Chen, C.S. (2012). A Microfabricated Platform to Measure and Manipulate the Mechanics of Engineered Cardiac Microtissues. Tissue Engineering Part A *18*, 910–919.

Bruusgaard, J.C., Johansen, I.B., Egner, I.M., Rana, Z.A., and Gundersen, K. (2010). Myonuclei acquired by overload exercise precede hypertrophy and are not lost on detraining. Proceedings of the National Academy of Sciences *107*, 15111–15116.

Charest, J.L., García, A.J., and King, W.P. (2007). Myoblast alignment and differentiation on cell culture substrates with microscale topography and model chemistries. Biomaterials *28*, 2202–2210.

Chiron, S., Tomczak, C., Duperray, A., Lainé, J., Bonne, G., Eder, A., Hansen, A., Eschenhagen, T., Verdier, C., and Coirault, C. (2012). Complex Interactions between Human Myoblasts and the Surrounding 3D Fibrin-Based Matrix. PLoS ONE *7*, e36173.

Clark, P., Coles, D., and Peckham, M. (1997). Preferential adhesion to and survival on patterned laminin organizes myogenesis in vitro. Exp Cell Res *230*, 275–283.

Cvetkovic, C., Raman, R., Chan, V., Williams, B.J., Tolish, M., Bajaj, P., Sakar, M.S., Asada, H.H., Saif, M.T.A., and Bashir, R. (2014). Three-dimensionally printed biological machines powered by skeletal muscle. Proceedings of the National Academy of Sciences *111*, 10125–10130.

Earle, A.J., Kirby, T.J., Fedorchak, G.R., Isermann, P., Patel, J., Iruvanti, S., Moore, S.A., Bonne, G., Wallrath, L.L., and Lammerding, J. (2020). Mutant lamins cause nuclear envelope rupture and DNA damage in skeletal muscle cells. Nat Mater *19*, 464–473.

Evano, B., and Tajbakhsh, S. (2018). Skeletal muscle stem cells in comfort and stress. Npj Regen Med *3*, 24.

Fink, J., Théry, M., Azioune, A., Dupont, R., Chatelain, F., Bornens, M., and Piel, M. (2007). Comparative study and improvement of current cell micro-patterning techniques. Lab Chip *7*, 672–680.

Gautel, M., and Djinović-Carugo, K. (2016). The sarcomeric cytoskeleton: from molecules to motion. Journal of Experimental Biology *219*, 135–145.

Ghibaudo, M., Di Meglio, J.-M., Hersen, P., and Ladoux, B. (2011). Mechanics of cell spreading within 3D-micropatterned environments. Lab Chip *11*, 805–812.

Gorji, A., Toh, P.J.Y., Ong, H.T., Toh, Y.-C., Toyama, Y., and Kanchanawong, P. (2021). Enhancement of Endothelialization by Topographical Features Is Mediated by PTP1B-Dependent Endothelial Adherens Junctions Remodeling. ACS Biomater. Sci. Eng. acsbiomaterials.1c00251.

Gribova, V., Liu, C.-Y., Nishiguchi, A., Matsusaki, M., Boudou, T., Picart, C., and Akashi, M. (2016). Construction and myogenic differentiation of 3D myoblast tissues fabricated by fibronectin-gelatin nanofilm coating. Biochemical and Biophysical Research Communications *474*, 515–521.

Hastings, R.L., Massopust, R.T., Haddix, S.G., Lee, Y. il, and Thompson, W.J. (2020). Exclusive vital labeling of myonuclei for studying myonuclear arrangement in mouse skeletal muscle tissue. Skeletal Muscle *10*, 15.

Huang, N.F., Lee, R.J., and Li, S. (2010). Engineering of aligned skeletal muscle by micropatterning. Am J Transl Res *2*, 43–55.

Iaizzo, P.A., and Durfee, W.K. (2011). Functional Force Assessment of Skeletal Muscles. In Springer Handbook of Medical Technology, R. Kramme, K.-P. Hoffmann, and R.S. Pozos, eds. (Berlin, Heidelberg: Springer Berlin Heidelberg), pp. 273–287.

Kalman, B., Picart, C., and Boudou, T. (2016). Quick and easy microfabrication of T-shaped cantilevers to generate arrays of microtissues. Biomed Microdevices *18*, 43.

Kim, D.-H., Lipke, E.A., Kim, P., Cheong, R., Thompson, S., Delannoy, M., Suh, K.-Y., Tung, L., and Levchenko, A. (2010). Nanoscale cues regulate the structure and function of macroscopic cardiac tissue constructs. Proceedings of the National Academy of Sciences *107*, 565–570.

Kural, M.H., and Billiar, K.L. (2013). Regulating tension in three-dimensional culture environments. Experimental Cell Research *319*, 2447–2459.

Lam, M.T., Sim, S., Zhu, X., and Takayama, S. (2006). The effect of continuous wavy micropatterns on silicone substrates on the alignment of skeletal muscle myoblasts and myotubes. Biomaterials *27*, 4340–4347.

Legant, W.R., Pathak, A., Yang, M.T., Deshpande, V.S., McMeeking, R.M., and Chen, C.S. (2009). Microfabricated tissue gauges to measure and manipulate forces from 3D

microtissues. Proc Natl Acad Sci U S A *106*, 10097–10102.

Lo, C.M., Wang, H.B., Dembo, M., and Wang, Y.L. (2000). Cell movement is guided by the rigidity of the substrate. Biophys J *79*, 144–152.

Maffioletti, S.M., Sarcar, S., Henderson, A.B.H., Mannhardt, I., Pinton, L., Moyle, L.A., Steele-Stallard, H., Cappellari, O., Wells, K.E., Ferrari, G., et al. (2018). Three-Dimensional Human iPSC-Derived Artificial Skeletal Muscles Model Muscular Dystrophies and Enable Multilineage Tissue Engineering. Cell Reports *23*, 899–908.

Mills, R.J., Parker, B.L., Monnot, P., Needham, E.J., Vivien, C.J., Ferguson, C., Parton, R.G., James, D.E., Porrello, E.R., and Hudson, J.E. (2019). Development of a human skeletal micro muscle platform with pacing capabilities. Biomaterials *198*, 217–227.

Osaki, T., Uzel, S.G.M., and Kamm, R.D. (2020). On-chip 3D neuromuscular model for drug screening and precision medicine in neuromuscular disease. Nat Protoc *15*, 421–449.

Pimentel, M.R., Falcone, S., Cadot, B., and Gomes, E.R. (2017). In Vitro Differentiation of Mature Myofibers for Live Imaging. JoVE 55141.

Plotnikov, S.V., Sabass, B., Schwarz, U.S., and Waterman, C.M. (2014). High-Resolution Traction Force Microscopy. In Methods in Cell Biology, (Elsevier), pp. 367–394.

Powers, J.D., Malingen, S.A., Regnier, M., and Daniel, T.L. (2021). The Sliding Filament Theory Since Andrew Huxley: Multiscale and Multidisciplinary Muscle Research. Annu. Rev. Biophys. *50*, 373–400.

Rao, L., Qian, Y., Khodabukus, A., Ribar, T., and Bursac, N. (2018). Engineering human pluripotent stem cells into a functional skeletal muscle tissue. Nat Commun *9*, 126.

Ronaldson-Bouchard, K., and Vunjak-Novakovic, G. (2018). Organs-on-a-Chip: A Fast Track for Engineered Human Tissues in Drug Development. Cell Stem Cell *22*, 310–324.

Saez, A., Buguin, A., Silberzan, P., and Ladoux, B. (2005). Is the mechanical activity of epithelial cells controlled by deformations or forces? Biophys J *89*, L52-54.

Saez, A., Ghibaudo, M., Buguin, A., Silberzan, P., and Ladoux, B. (2007). Rigidity-driven growth and migration of epithelial cells on microstructured anisotropic substrates. Proceedings of the National Academy of Sciences *104*, 8281–8286.

Sakar, M.S., Neal, D., Boudou, T., Borochin, M.A., Li, Y., Weiss, R., Kamm, R.D., Chen, C.S., and Asada, H.H. (2012). Formation and optogenetic control of engineered 3D skeletal muscle bioactuators. Lab Chip *12*, 4976–4985.

Strale, P.-O., Azioune, A., Bugnicourt, G., Lecomte, Y., Chahid, M., and Studer, V. (2016). Multiprotein Printing by Light-Induced Molecular Adsorption. Adv. Mater. *28*, 2024–2029.

Tan, J.L., Tien, J., Pirone, D.M., Gray, D.S., Bhadriraju, K., and Chen, C.S. (2003). Cells lying on a bed of microneedles: An approach to isolate mechanical force. Proceedings of the National Academy of Sciences *100*, 1484–1489.

Théry, M. (2010). Micropatterning as a tool to decipher cell morphogenesis and functions. Journal of Cell Science *123*, 4201–4213.

Trichet, L., Le Digabel, J., Hawkins, R.J., Vedula, S.R.K., Gupta, M., Ribrault, C., Hersen, P., Voituriez, R., and Ladoux, B. (2012). Evidence of a large-scale mechanosensing mechanism for cellular adaptation to substrate stiffness. Proceedings of the National Academy of Sciences *109*, 6933–6938.

Walker, M., Godin, M., and Pelling, A.E. (2018). A vacuum-actuated microtissue stretcher for long-term exposure to oscillatory strain within a 3D matrix. Biomed Microdevices *20*, 43.

Yin, H., Price, F., and Rudnicki, M.A. (2013). Satellite Cells and the Muscle Stem Cell Niche. Physiological Reviews *93*, 23–67.

Zhang, H., Wen, J., Bigot, A., Chen, J., Shang, R., Mouly, V., and Bi, P. (2020). Human myotube formation is determined by MyoD–Myomixer/Myomaker axis. Sci. Adv. *6*, eabc4062.